Earth and Planetary Science Letters 620 (2023) 118355

Contents lists available at ScienceDirect

Earth and Planetary Science Letters

journal homepage: www.elsevier.com/locate/epsl

Timing and drivers of exhumation and sedimentation in the eastern Peruvian Andes: Insights from thermokinematic modelling

Victoria M. Buford Parks [a], Nadine McQuarrie [a,*], Sarah Falkowski [b], Nicholas D. Perez [c], Todd A. Ehlers [b,1]

[a] University of Pittsburgh, Department of Geology and Environmental Science, 4107 O'Hara Street, Pittsburgh, PA 15261, USA
[b] University of Tübingen, Department of Geosciences, Schnarrenbergstr. 94-96, 72076 Tübingen, Germany
[c] Texas A&M University, Department of Geology and Geophysics, MS 3115, College Station, TX 77843, USA

ARTICLE INFO

Article history:
Received 15 December 2022
Received in revised form 10 August 2023
Accepted 13 August 2023
Available online xxxx
Editor: A. Webb

Keywords:
Peru
central Andes
thermochronology
climate
tectonics
incision

ABSTRACT

This study assesses the impact of fold-thrust belt driven deformation on the topographic evolution, bedrock exhumation and basin formation in the southeastern Peruvian Andes. We do this through a flexural and thermokinematically modelled balanced cross-section. In addition, published thermochronology samples from low-elevation (river canyons) and high-elevation (interfluves) and Cenozoic sedimentary basin datasets along the balanced cross-section were used to evaluate the age, location, and geometry of fault-driven uplift, as well as potential relationships to the timing of ~2 km of canyon incision. The integrated structural, thermochronologic, and basin data were used to test the sensitivity of model results to various shortening rates and durations, a range of thermophysical parameters, and different magnitudes and timing of canyon incision. Results indicate that young apatite (U-Th)/He (AHe) canyon samples from ~2 km in elevation or lower are consistent with river incision occurring between ~8–2 Ma and are independent of the timing of ramp-driven uplift and accompanying erosion. In contrast, replicating the young AHe canyon samples located at >2.7 km elevation requires ongoing ramp-driven uplift. Replicating older interfluve cooling ages concurrent with young canyon ages necessitates slow shortening rates (0.25–0.6 mm/y) from ~10 Ma to Present, potentially reflecting a decrease in upper plate compression during slab steepening. The best-fit model that reproduces basin ages and depositional contacts requires a background shortening rate of 3–4 mm/y with a marked decrease in rates to ≤0.5 mm/y at ~10 Ma. Canyon incision occurred during this period of slow shortening, potentially enhanced by Pliocene climate change.

1. Introduction

The balance between climate and tectonics in shaping mountain morphology continues to be debated in the Central Andes of South America (e.g., Jeffery et al., 2013; Lease and Ehlers, 2013; Masek et al., 1994; Montgomery et al., 2001; Whipple and Gasparini, 2014). In the southern Peruvian Andes, high broad interfluves appear to be extensions of the northern Andean Plateau. These interfluves are separated by deep fluvial canyons carved into both the eastern and western edges of the plateau. Previous studies have suggested that this incision is driven by marked changes in climate (Jeffery et al., 2013; Lease and Ehlers, 2013), by large-scale plateau surface uplift via loss of dense lithosphere or addition of lower crustal material (Garzione et al., 2017; Hoke et al., 2007; Schildgen et al., 2007), or by capture of an endorheic basin (Gérard et al., 2021a,b). These processes may also be accompanied by structurally-driven uplift due to subsurface ramps or surface-breaking faults, potentially increasing erosional exhumation (e.g., Whipple and Tucker, 1999; Gasparini and Whipple, 2014). Disentangling the relative contributions of these drivers remains challenging and is the focus of this study.

Flexural and thermal kinematic models tied to thermochronometric cooling ages can help differentiate between proposed drivers of exhumation. Flexural kinematic models of deformation seek to replicate the observed geology at the surface, measured foreland basin thickness, age and location, and topography that reflects structural uplift variations in space and time (Mc-

* Corresponding author.
E-mail addresses: vmbparks@gmail.com (V.M. Buford Parks), nmcq@pitt.edu (N. McQuarrie), sarah.falkowski@uni-tuebingen.de (S. Falkowski), ndperez@tamu.edu (N.D. Perez), todd.ehlers@glasgow.ac.uk (T.A. Ehlers).
[1] Now at: University of Glasgow, School of Geographical and Earth Sciences, Glasgow, UK.

https://doi.org/10.1016/j.epsl.2023.118355

Quarrie et al., 2019; Braza and McQuarrie, 2022; Ghoshal et al., 2023). For both structurally-driven uplift and/or climate-driven incision, flexural kinematic models are required to reproduce both modern topography and the geology exposed at the surface. Mismatches in topography, particularly elevations at the eastern edge of the plateau, may indicate large-scale, plateau uplift is needed to achieve modern elevations of ~4 km (Kar et al., 2016). The across-strike pattern of thermochronologic ages (Falkowski et al., 2023), is also predicted to vary systematically based on the dominant driver of exhumation. Structurally-driven uplift is predicted to yield the youngest ages at a surface-breaking fault, or over an active thrust ramp with ages increasing in the direction of transport (Lock and Willett, 2008; McQuarrie and Ehlers, 2017; Rak et al., 2017). This exhumation signal will be recorded by both canyon and interfluve samples. In contrast, incision driven by drainage basin capture, large-scale plateau surface uplift or a climatic shift from warmer and dryer Pliocene to cooler but wetter present-day (Lease and Ehlers, 2013; Mutz et al., 2018) is predicted to have apatite (U-Th)/He ages <5 Ma only in the deepest portions of the canyon, while interfluves would record older ages from the last phase of structurally-driven exhumation. Upper portions of the canyon (<1.5 km beneath interfluve) and higher-temperature thermochronometers would record an integrated signal of both.

In this study, we evaluate the timing, rate, and location of structural shortening in the deeply incised San Gabán canyon in southern Peru through a sequentially-deformed, flexural-kinematic balanced cross-section integrated with a thermo-kinematic model. This approach predicts a topographic and sedimentary basin evolution that facilitates the comparison of published thermochronometric and basin ages to modelled ages resulting from balanced cross-section geometry and kinematics. We use this model to constrain the location, magnitude, and age of fault-driven uplift, evaluate permissible shortening rates, and assess whether deformation alone is sufficient to explain both modern topography and thermochronometric ages or whether potential plateau uplift and/or climate-enhanced incision is also required to match observed datasets.

2. Background

2.1. Geologic framework

The Central Andes in southern Peru are NW-trending, ~400 km wide, and consist from west to east of a subduction trench, Neogene Western Cordillera (WC) magmatic arc, largely internally drained plateau (the Altiplano - AP), Eastern Cordillera (EC), Subandean Zone (SA), and modern foreland basin. Southern Peru marks the northern extent of the Central Andean Plateau, defined as the >3.5 km elevation region encompassing the AP, EC, and WC. The low relief AP contains 4–6 km, and locally up to 10 km, of synorogenic Cenozoic sediment in Peru (Fig. 1) (Carlotto, 2013; Horton, 2018; Horton et al., 2015; Perez and Horton, 2014; Sundell et al., 2018). The EC, a hinterland fold-and-thrust belt with surface exposures of Paleozoic–Mesozoic strata, encompasses several distinct structural zones (Figs. 1, 2). The backthrust belt primarily exposes Cretaceous strata in Peru in a series of tight folds and faults. The Macusani Structural Zone, which has an oblique orientation of faults and folds in Carboniferous–Permian strata, has been attributed to Andean-age re-activation of late Paleozoic rift structures (Clark et al., 1990; Sempere et al., 2002; Perez et al., 2016a). Finally, in the Cordillera de Carabaya, broadly folded Ordovician and Devonian exposures, intruded by a suite of Permo-Triassic plutons, mark the northeastern extent of the EC. The SA is a thin-skinned frontal belt with the most recent deformation, exposing the Cretaceous through Cenozoic strata. The potential subsurface geometry of southern Peru (13–15°S) was presented in a balanced cross-section by Perez et al. (2016b) (Fig. 2; Text S1).

3. Previous related work

3.1. Regional sedimentary basin synthesis

Synorogenic sedimentation in the Altiplano of southern Peru is preserved in several segregated basins that show components of a shared depocenter history as well as unique depozones with respect to age, thickness, and composition (Carlotto, 2013; Horton, 2018; Horton et al., 2015; Kar et al., 2016; Perez and Horton, 2014; Saylor and Horton, 2014; Sundell et al., 2018). The Ayaviri Basin (Horton et al., 2015) is subdivided into the Llalli and Tinajani sub-basins and separated by the Pasani Fault (Figs. 1, 3). In the Llalli sub-basin, the oldest Andean synorogenic deposits are sediments of the western-derived >3–5 km-thick Eocene–Oligocene San Jeronimo (Puno) Group, which unconformably overlay Cretaceous strata (Horton et al., 2015). Further east, in the Tinajani sub-basin, the ~1.3-km-thick Puno Group is dated between ~29 and 24 Ma. The Puno Group is in depositional contact with the Jurassic–Cretaceous Muni Formation and the Silurian/Devonian Chagrapi Formation at its eastern and northeastern edges (Perez and Horton, 2014). On the southwestern side of the Tinajani sub-basin, the Tinajani Formation is in contact with the Lower Ordovician San Jose Formation (Perez and Horton, 2014). Overlain on the Puno Group in the Tinajani sub-basin is the Neogene Tinajani Formation, which accumulated >1.1 km thickness between 24 and 17 Ma. Several angular unconformities are preserved in exposures in the Ayaviri Basin (28–26 Ma) and Tinajani (18–16 Ma) sub-basins that highlight faulting and associated differential uplift during those times (Perez and Horton, 2014).

3.2. San Gabán thermochronology

Published thermochronology data throughout southern Peru (59 samples and 104 ages; Table S1) are sourced from Ordovician age quartzites (n=5), Permo-Triassic plutons (n=36), Permo-Triassic volcanic rocks (n=10), Cretaceous strata from the SAZ (n=4) and the western EC (n=1), and synorogenic rocks in the AP (n=2) and SAZ (n=1) (Fig. 1). Nearly 65% of the data are concentrated in the ~2 km-deep canyons that dissect the plateau edge (Clark et al., 1990; Falkowski et al., 2023; Farrar et al., 1988; Kontak et al., 1987, 1990a; Lease and Ehlers, 2013; Perez, 2015; Perez et al., 2016b). Samples from high elevation interfluves (n=12; Falkowski et al., 2023; Perez et al., 2016b) provide similar structural positions, but contrasting elevations to canyon samples (Figs. 1, 4). Thermochronometers used in this study include apatite and zircon (U-Th)/He (AHe and ZHe), apatite and zircon fission track (AFT and ZFT) and biotite $^{40}Ar/^{39}Ar$ (BAr) ages. These samples broadly record cooling through 68 °C (Farley, 2000), 110 °C (Ketcham et al., 2007), 180 °C (Reiners et al., 2004), 240 °C (Brandon et al., 1998), and 350 °C (Grove and Harrison, 1996), respectively. BAr (49–36 Ma) and ZFT (29–36 Ma) ages (Kontak et al., 1990b; Falkowski et al., 2023) from canyon plutons argue for exhumation initiating between 50 and 40 Ma. BAr ages between 89 and 122 Ma are interpreted to represent partial resetting between pluton age (~260–200 Ma; Kontak et al., 1990a) and the onset of exhumation. Reset ZHe ages range from 48 Ma to 6 Ma. Partially reset and detrital ZHe ages are from the western EC (73–248 Ma) and Neogene SA (26–284 Ma). Reset AFT and AHe ages range from 50–7.3 Ma and 32–1.9 Ma, respectively (Fig. 4; Table S1).

4. Methods

The cross-section of Perez et al. (2016b) was modified and extended westward to account for the geometry of structures

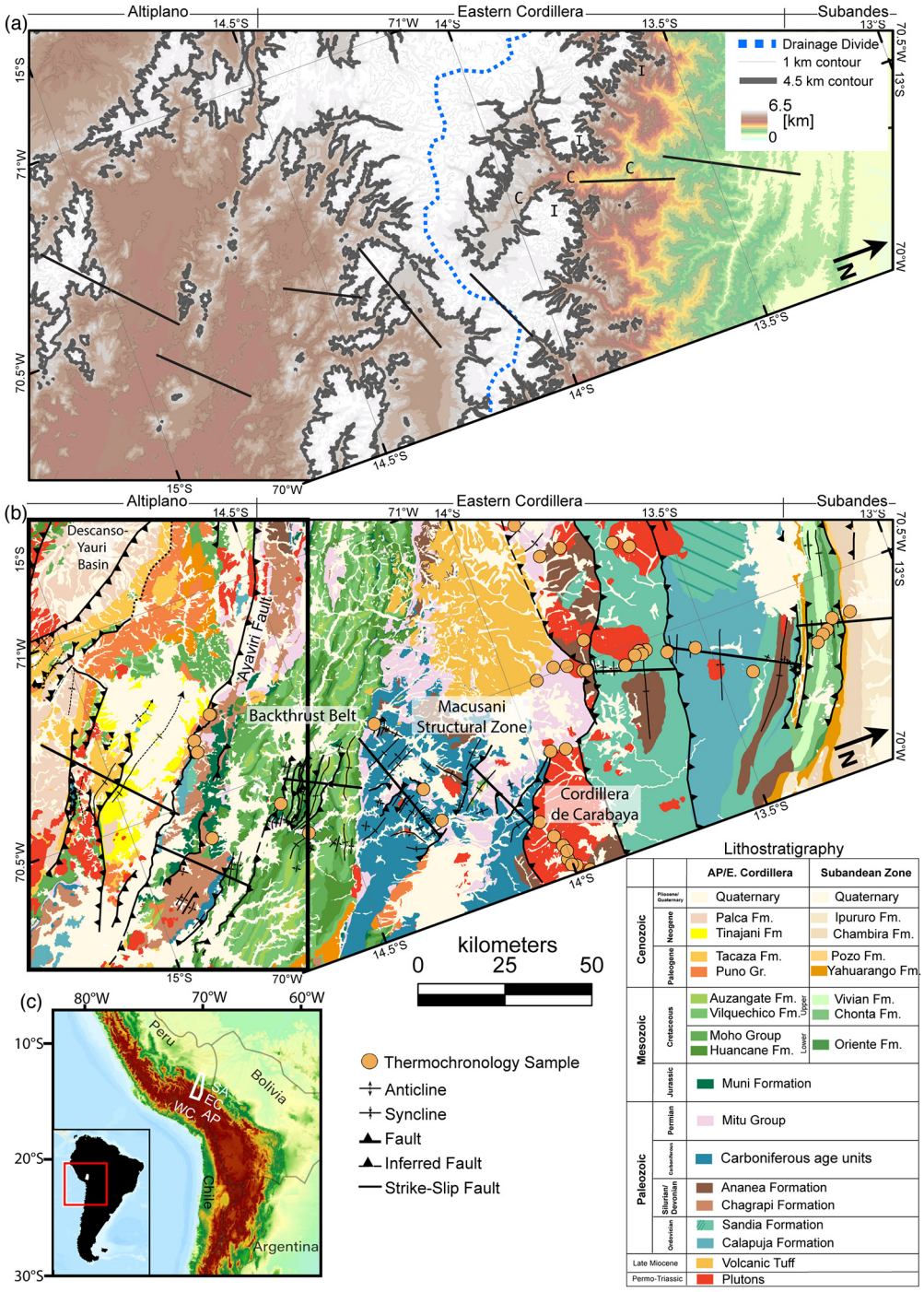

Fig. 1. (a) Topographic map (based on ASTER GDEM) of the study area with bolded 4500 m contour and drainage divide between systems that drain northward and southward, I=interfluve, C=canyon. (b) Geologic map (modified from Sánchez and Zapata (2003), Cerrón and Chacaltana (2003), Monge Miguel and Montoya Pérez (2003) and Perez et al. (2016b) with published thermochronology sample locations (Clark et al., 1990; Falkowski et al., 2023; Farrar et al., 1988; Kontak et al., 1987, 1990a; Lease and Ehlers, 2013; Perez, 2015; Perez et al., 2016b) (inset box corresponds to Fig. 4). Black lines in (a) and (b) represent balanced cross-section lines. The lines are proximal to field observations and oriented normal to the structural trend, which changes from ~N 20 E to N 60 E in the Macusani Structural Zone (Perez et al., 2016a), resulting in multiple breaks in the section. Breaks are positioned at major structures (Perez et al., 2016b). (c) Digital topography of the Central Andes, WC is Western Cordillera, AP is Altiplano, EC is Eastern Cordillera, SA is Subandean Zone. White box marks location of (a) and (b).

in the AP (Figs. 2, 3). Flexural-kinematic modelling sequentially displaced each fault and associated strata to reproduce the cross-section geometry, sedimentary basins, and topography. The successful flexural-kinematic model is input into thermal models to predict thermochronometric ages (Braza and McQuarrie, 2022; Buford Parks and McQuarrie, 2019; Rak et al., 2017).

4.1. Flexural-kinematic model

The modified Perez et al. (2016b) cross-section and a 0.5 × 0.5 km grid of unique points were displaced in ~10 km increments to track deformation in time and space (Fig. 5, Supplementary video). Following each deformation increment, the isostatic response of the uplifted topographic surface was calculated us-

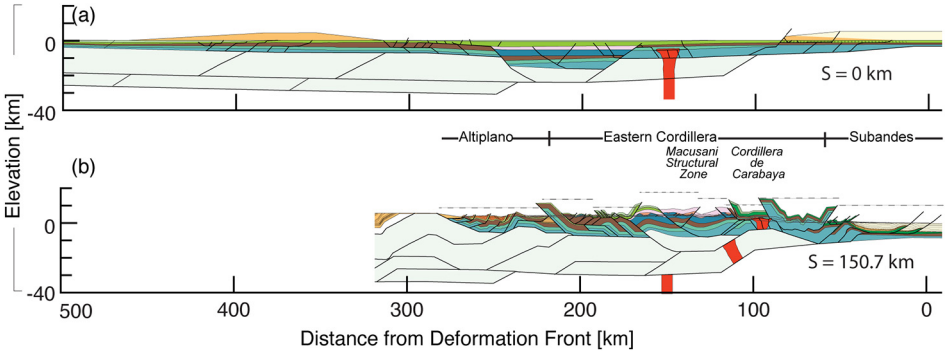

Fig. 2. Balanced cross-section modified from Perez et al. (2016b) (a) restored and (b) deformed. Dashed lines represent breaks in section (Fig. 1). The Altiplano portion of the section was added in this study. *S* signifies shortening magnitude.

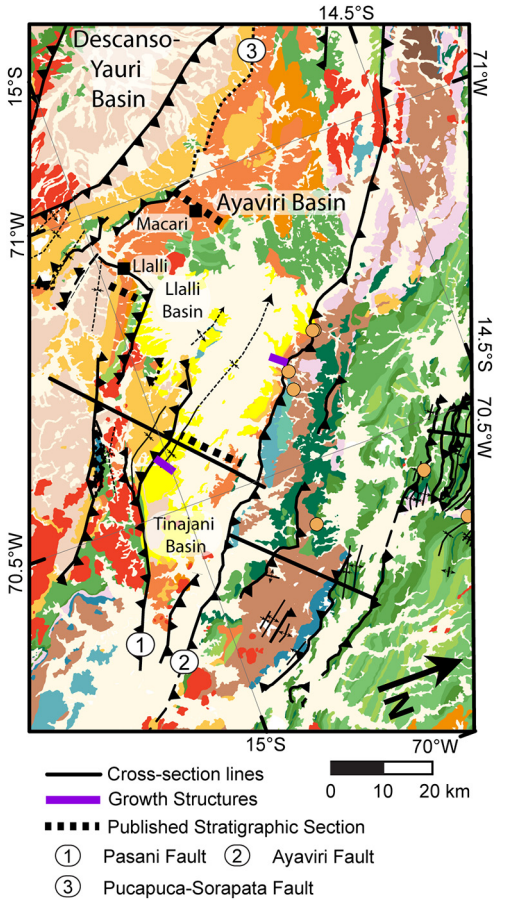

Fig. 3. Geologic map of the Altiplano in southern Peru (modified from Sánchez and Zapata (2003), Cerrón and Chacaltana (2003), Perez and Horton (2014), and Perez et al. (2016b)). Location shown in Fig. 1.

ing the difference between the deformed and prior topographic surfaces. Post-isostatic loading, the new topographic surface is estimated by assuming topography increases from the deformation front at a westward increasing slope (α), everywhere that has undergone surface uplift, typically 1–3°. Erosion occurs above the new topographic surface, and deposition below 0 km (McQuarrie and Ehlers, 2015; Rak et al., 2017; Gilmore et al., 2018). The resulting 2-D topographic profile following each deformation increment represents mean topography. For the last ~17 km of deformation, we also track the highest potential topography (interfluve) and lowest (canyon). Tracking topographies representative of interfluve and canyon elevations during the last ~8 My of Subandean shortening allows us to evaluate the sensitivity of modelled thermochronometric ages to elevation differences and when relief was established. A series of iterative flexural-kinematic models systematically altered load density, effective elastic thickness (EET), and fault kinematics to find a solution that reproduced mapped surface geology and basin depths (Table 1; Text S2).

Table 1
Thermal parameters for *Pecube-D* modelling. Details of these parameters are provided in the Supplementary Materials.

Parameter	Input Value
Effecting Elastic Thickness (EET)	25–80 km
Crustal density	2500 kg/m^3
Sedimentary basin density	2100 kg/m^3
Mantle density	3300 kg/m^3
Constant shortening rates	3 mm/y
Variable shortening rate 50–10 Ma	4 mm/y
Variable shortening rate 10–0 Ma	0.25–0.5 mm/y
Surface radiogenic heat production (A_o)	2.0–3.0 μW/m^3
e-folding depth (Ef)	12 km
Thermal Conductivity	2.5 W/m/K
Specific Heat	800 J/kg/K
Model Base	110 km
Temperature at base	1300 °C
Temperature at surface	23 °C
Atmospheric Lapse Rate	4.0 °C/km
Kinematic grid spacing	0.5 km x 0.5 km
Displacement Increment	~8–10 km
Model Domain (xyz)	600 km x 5 km x 110 km
Horizontal node spacing	0.5 km
Vertical node spacing	1.0 km
Model start time (thermal initiation)	100 Ma
Deformation start time	50–40 Ma

4.2. Thermal model

To evaluate if the cross-section geometry can reproduce the measured thermochronometric ages in the region, the grid of unique points and surface topography from each step in the flexural-kinematic model was used, in combination with thermophysical parameters (Table 1), as the input for a modified version of the advection-diffusion thermal modelling code *Pecube*, *Pecube-D* (Braun, 2002, 2003; McQuarrie and Ehlers, 2015; Whipp et al., 2007; Ehlers, 2023). *Pecube-D* predicts thermochronometer ages based on modelled thermal histories and prescribed kinetic parameters (Text S3). The displacement grids from the *Move* model become velocity fields by assigning time to each deformation step. The velocity fields are used to calculate the advective component of heat transfer as a function of fold-and-thrust belt evolution. We evaluate the sensitivity of model results to 1) surface radiogenic heat production (Text S3), 2) age of incision, 3) initiation ages of 50, 45 and 40 Ma based on 49–36 Ma BAr ages in the Cordillera de Carabaya (Kontak et al. 1990a, 1990b) (Figs. 1, 4), and 4) variations in shortening rate. Table 1 provides details of the

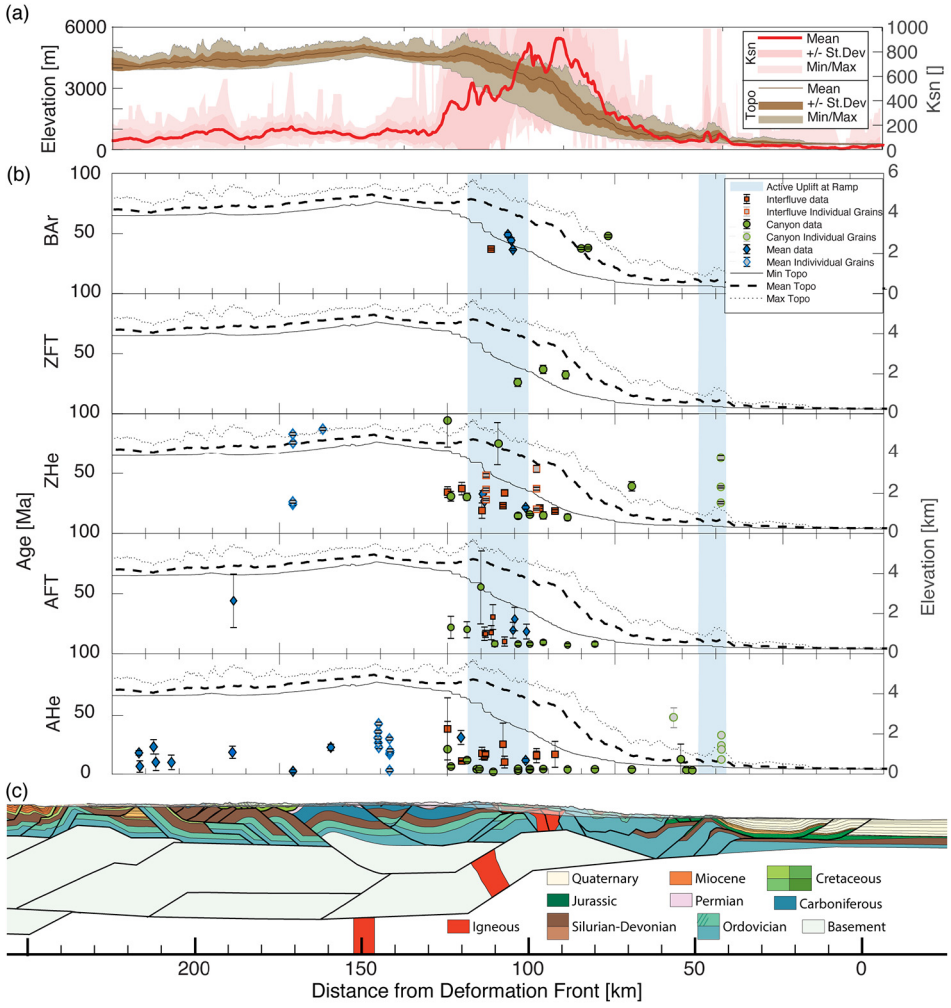

Fig. 4. Cross-sectional projection of thermochronology data in our study area; (a) topography (shades of brown) and normalized river steepness (Ksn- shades of red) from a 50-km-wide swath (25 km on either side of the cross-section), and a concavity of 0.5 to calculate a running average of Ksn values (Eizenhöfer et al., 2019); (b) thermochronology data for biotite $^{40}Ar/^{39}Ar$ (BAr), zircon fission track (ZFT) zircon (U-Th)/He (ZHe), apatite fission track (AFT), and apatite (U-Th)/He (AHe) (Clark et al., 1990; Falkowski et al., 2023; Farrar et al., 1988; Kontak et al., 1987, 1990a; Lease and Ehlers, 2013; Perez, 2015; Perez et al., 2016b); grayed markers identify individual grain ages where no mean age has been computed; (c) balanced cross-section. The x-axis on all three panels is the same. The region of high normalized channel steepness (Ksn), and youngest cooling ages are located at and directly NE of the basement footwall ramp (100–120 km).

model parameters, thermophysical properties, and boundary conditions used (Text S2; S3). The thermal model was permitted to equilibrate crustal temperatures for 50 My prior to the initiation of deformation resulting in 50 Ma modelled ages before the initiation of shortening (Fig. 5). Modelled ages are considered partially reset if their ages fall between the model start time (~100 Ma at the end of the model) and the oldest age of deformation experienced by that portion of the model (Fig. 5). The source code and a singularity container for the version of *Pecube-D* used in this study is freely available in Ehlers (2023).

We limit the thermochronometer data used in this study to within 50 km of the cross-section to exclude lateral variability in structural history. They are projected onto the section maintaining their relationship to mapped structures (Fig. S6). When AHe and ZHe ages are reset, they are plotted as mean ages, when they are partially or unreset or do not represent a cohesive population, individual grain (single-grain) ages are plotted (Falkowski et al., 2023). All ages are plotted with 2σ-error (Fig. 4) (Table S1). Although plotted to highlight the location and age of early exhumation, the BAr ages are not modelled. Interfluve samples (n=16) are from elevations of 3700 to 5042 m and are within ~750 m of the maximum elevation along strike. The canyon samples (n=33) were collected close to the Rio San Gabán and range in elevation from 484 to ~3300 m. They are at least 750 m lower in elevation than along-strike of the interfluve samples. The separation of interfluve and canyon ends when canyon-interfluve relief drops to <1.5 km. These samples, as well as samples collected below 750 m of maximum elevation are mean topographic samples (n=10).

5. Results

5.1. Balanced cross-section

The existing Perez et al. (2016b) cross-section covered the SA through the EC and stops at the Ayaviri Fault, the boundary between the EC and the AP. The original cross-section of Perez et al. (2016b) argued for 130 km (38%) of Cenozoic orogen shortening. We extended the Perez et al. (2016b) section southwestward by constructing the geometry and amount of shortening from the western edge of the AP to the Ayaviri Fault based on the available sedimentologic constraints and mapped geologic strata (Figs. 1–3). The SA geometry and shortening were also modified to make the cross-section geometry more consistent with mapping and available seismic reflection data (Perez et al., 2016b).

The updated cross-section proposes basement thrust sheets beneath the AP that are required to balance upper crustal shortening

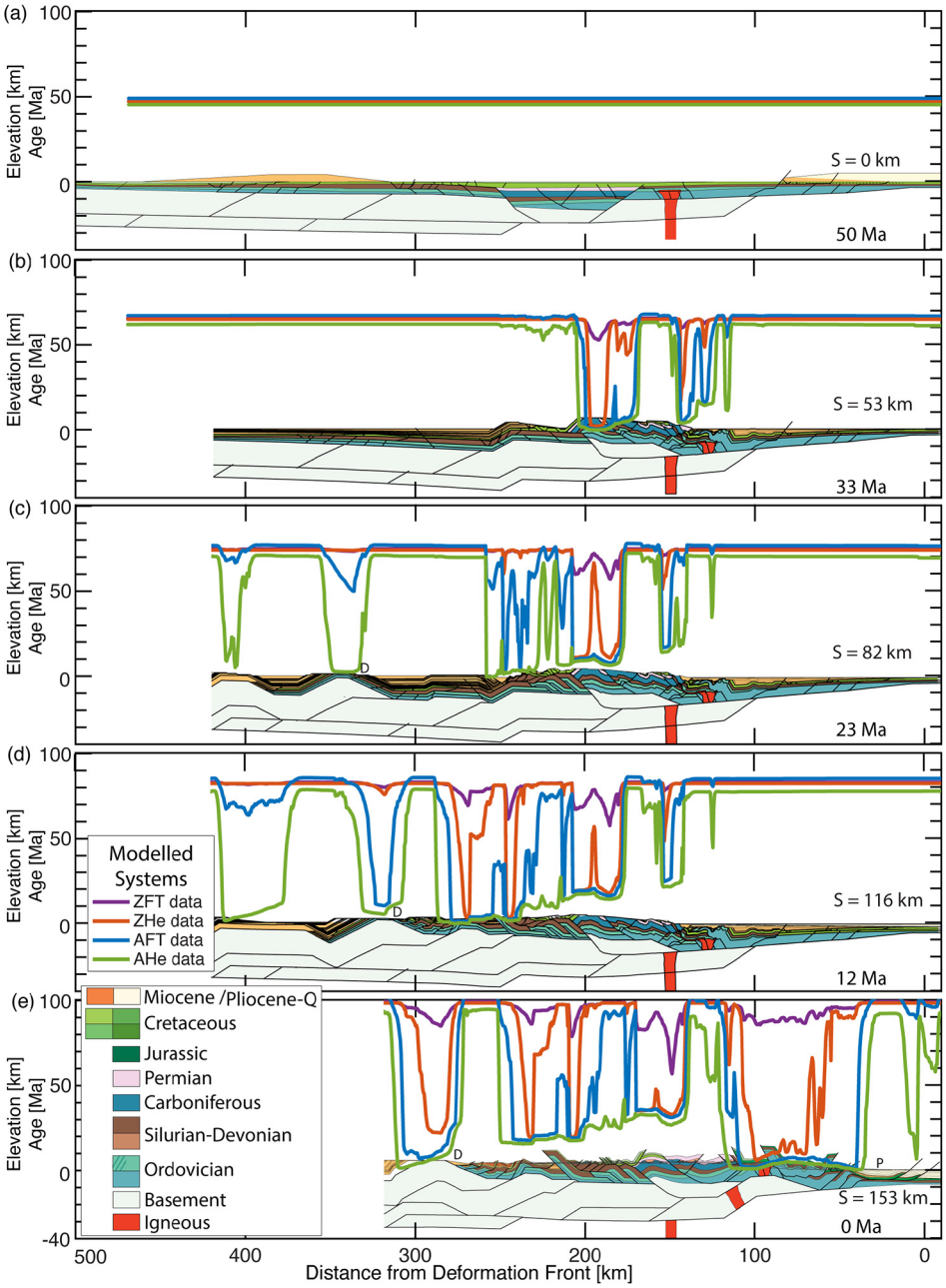

Fig. 5. Sequential deformation and modelled thermochronometric ages as a function of a constant shortening rate (3 mm/y) and surface radiogenic heat production values of $A_o = 2.7$ μW/m^3 and 12 km e-folding depth. D=Descanso region on panels c-e; P=Punquiri syncline on panel e.

(Fig. 2). The faulted footwall and hanging wall ramps of the northeastern basement faults under the Altiplano are constrained by the mapped unconformity between Tinajani and lower Ordovician on the border between the Tinajani and Llalli sub-basins (Fig. 3; Text S1). A second southwestern basement fault is interpreted southwest of the Llalli sub-basin to provide the uplift needed to define the edge of the basin and to distribute shortening to the series of faults that repeat the Paleozoic through Cretaceous section and partition deformation in the sub-basins (e.g., Horton et al., 2015). A deeper basement fault system is proposed to maintain topographic uplift and a western sediment source (Sundell et al., 2018) to the basins (Fig. 2).

The surface-breaking structures in the AP (primarily the Pasani and Llalli faults) accommodate 16 km of shortening and are balanced at depth via shortening along the two basement thrusts. The final cross-section covers the SA, EC, and AP at 13–15°S and constrains 150 km (35%) shortening.

5.2. Sequential deformation, thermochronometric ages, and basin formation

The following sections describe the relationship of cross-section geometry and kinematics to the resulting pattern of deformation, basin formation and modelled thermochronometric ages assuming a constant shortening rate of ~3 mm/y (Villegas-Lanza et al., 2016) and a 50 Ma onset of deformation.

5.2.1. Cordillera de Carabaya and the Macusani Structural Zone (50–33 Ma)

At 50 Ma, modelled deformation was initiated in the San Gabán region of the Cordillera de Carabaya located in the northeastern

portion of the EC (Fig. 1). The development of a west-verging duplex (~140 km, Fig. 5b) was balanced at depth by shortening along the basement thrust sheet beneath the EC. By 33 Ma, duplex formation produced ~15 Ma modelled AFT and AHe ages. The active basement ramp to the southwest (~170–200 km) produced topographic uplift and exhumation with 0 Ma thermochronometric model ages at the ramp (200 km, Fig. 5a, b) that increase northeastward to 10 Ma. Modelled shortening has also propagated southwestward into the Macusani Structural Zone (Fig. 5b). The modelled deformation and associated flexural loading produced two synorogenic flexural basins, one on either side of the uplifted, deformed topography (western basin: 400–250 km, eastern basin: 130–20 km in Fig. 5b), precursors to the AP and SA depocenters respectively. The flexural basin is deeper on the southwestern side, reaching a maximum of 5.7 km depth (versus ~2 km on the northeastern side), driven by topographic uplift over basement structures.

5.2.2. Eastern Cordillera backthrust belt and Altiplano sedimentation (33–23 Ma)

By 23 Ma, deformation propagated across the backthrust belt and facilitated ~7 km of predicted sedimentation in the AP Basin from 40–23 Ma (Fig. 5c). Model predicted shortening across the EC backthrust belt exhumed the proximal synorogenic basin deposited before 23 Ma, resulting in 0–10 Ma modelled AHe ages and partially reset AFT ages between ~285 and 250 km (Fig. 5c). The shortening in the backthrust belt is balanced at depth with basement thrust sheets beneath the AP, specifically, the western basement thrust sheet that defines the WC-AP boundary near Descanso (350–325 km, label D, Fig. 5c, d). Shortening and uplifting of this basement structure fully reset the predicted AHe ages, partially reset the AFT ages, and provide a western sedimentation source to the AP.

5.2.3. Altiplano (23–12 Ma)

The basement thrust sheet under the AP (270–280 km) partitioned the AP flexural basin that initially developed as a contiguous system (400–250 km Fig. 5b, c) into two separate basins (the Llalli and Tinajani sub-basins) with independent sedimentation histories from 23–17 Ma (Fig. 5d). This basement structure also lifted lower Paleozoic strata to produce an angular unconformity (Fig. 5c, d) in accordance with sedimentologic and stratigraphic data (Horton et al., 2015; Perez and Horton, 2014). Motion on this basement fault is balanced by displacement on the Ayaviri Thrust from ~23–17 Ma (assuming constant shortening rates). Shortening within the AP elevates surface structures to modern elevations (~4 km). The shortening in the AP on surface-breaking and subsurface structures facilitated erosional exhumation to reset AHe and AFT ages across nearly the entire AP except between ~285–310 km, a region between the two basement ramps that focused topographic uplift and exhumation (Fig. 5d). The modelled reset AHe age pattern across the AP merges with the EC, and the boundary between them is not visible in the model predicted AHe ages. By the end of AP shortening, 3 km of predicted sediment accumulation was preserved in the Ayaviri and Llalli sub-basins, consistent with previously reported stratigraphic thicknesses (Horton et al., 2015; Perez and Horton, 2014), and an additional ~2 km of predicted sediment was accumulated in the Subandean flexural basin. This created up to 4.5 km of synorogenic sedimentation before SA deformation initiation (~12 Ma).

5.2.4. Subandean zone (12–0 Ma)

Shortening migrated from the AP to the SA at ~12 Ma and propagated from southwest to northeast (Fig. 5d, e). Motion on the easternmost basement thrust lifted the EC and transferred shortening to faults that repeat the Paleozoic section in a northeastward propagating duplex. This shortening is balanced by a duplex in Cretaceous age rocks that uplifts and folds Upper Cretaceous and younger rocks at the surface. Ongoing synorogenic sedimentation in the SA adds up to ~3 km of sediment in the northeasternmost reaches of the modelled basin to a final foreland basin depth of ~4.5 km.

At the end of the SA shortening (Fig. 5e), model predicted AHe ages are 0 Ma over the active SA basement ramp (~125 km, Fig. 5e) and increase in age to 5 Ma in the direction of transport between 90 and 70 km before becoming younger again (~0 Ma) at the western edge of the Punquiri syncline (labelled P, ~50 km) before ages return to being unreset. Predicted AFT ages are fully reset over a narrower window (~130–80 km) and are slightly older (~2–7 My) than predicted AHe ages. Predicted ZHe ages are the youngest (7 Ma) at the ramp and fluctuate between 15–10 Ma over the uplifted basement thrust (100–75 km) before increasing to unreset ages at ~60 km (Fig. 5e).

5.3. Impact of canyon incision depth and rate on thermochronometer results

Here, we evaluate the effects of varying canyon incision timing and magnitudes on predicted cooling ages. We generate canyon, and interfluve topographies consistent with topographic uplift over ramps and mapped geology (Fig. 6) for the last 17, 6, 4, 2, 1, or 0.5 km of shortening (corresponding to periods of 5.67, 3.3, 1.3, or <0.65 Ma at constant rates). Models were conducted using a constant shortening rate of 3.0 mm/y and surface radiogenic heat production $A_o = 2.7\ \mu W/m^3$ with an e-folding depth of 12 km. The model-predicted thermochronometric ages were compared to measured ages sampled from canyon, mean, and interfluve locations. Results indicate that AHe and AFT ages between 115 and 50 km are the same, regardless of incision magnitude (Fig. 6c, d). The modelled canyon and interfluve AHe and AFT ages (Fig. 6b) show the same reset pattern as the predicted ages for the mean topography (Figs. 5, 6b). The only notable difference is at 120–125 km, where predicted AFT and AHe interfluve ages are older than canyon ages.

In contrast, results from predicted ZHe ages show that interfluve ages (20–80 Ma) are markedly older than the canyon ages (7–12 Ma). This suggests that at a constant rate of shortening (3 mm/y), ZHe is the only thermochronometer sensitive to different incision levels (Fig. 6b). Varying the age of incision from 5.67 to 3.33 and 1.33 Ma shows virtually indistinguishable predicted thermochronometric ages (Fig. S2).

While measured ages for all three thermochronometers record older ages at higher elevations (Fig. 7), predicted AFT and AHe ages at a constant shortening rate show very limited variation in age with incision magnitude. In addition, the predicted canyon and mean topography ZHe ages are younger than the measured ages. For the predicted AFT ages, the canyon, mean topography, and interfluve ages are younger than the measured ages between 125 and 90 km distance. While the predicted canyon AHe ages match the measured ages, the predicted interfluve AHe ages are 10–15 My younger than the measured interfluve ages. These mismatches show that incision during constant shortening rates cannot replicate the measured AHe, AFT, and ZHe ages.

5.4. Effect of shortening rate on modelled ages (SA and EC)

We evaluated a suite of shortening rates to assess whether slower velocities could differentiate between predicted and observed AHe and AFT ages for canyon and interfluve topographies. The models tested slowed SA shortening rates (0.25, 0.5, 0.75, 1.0,

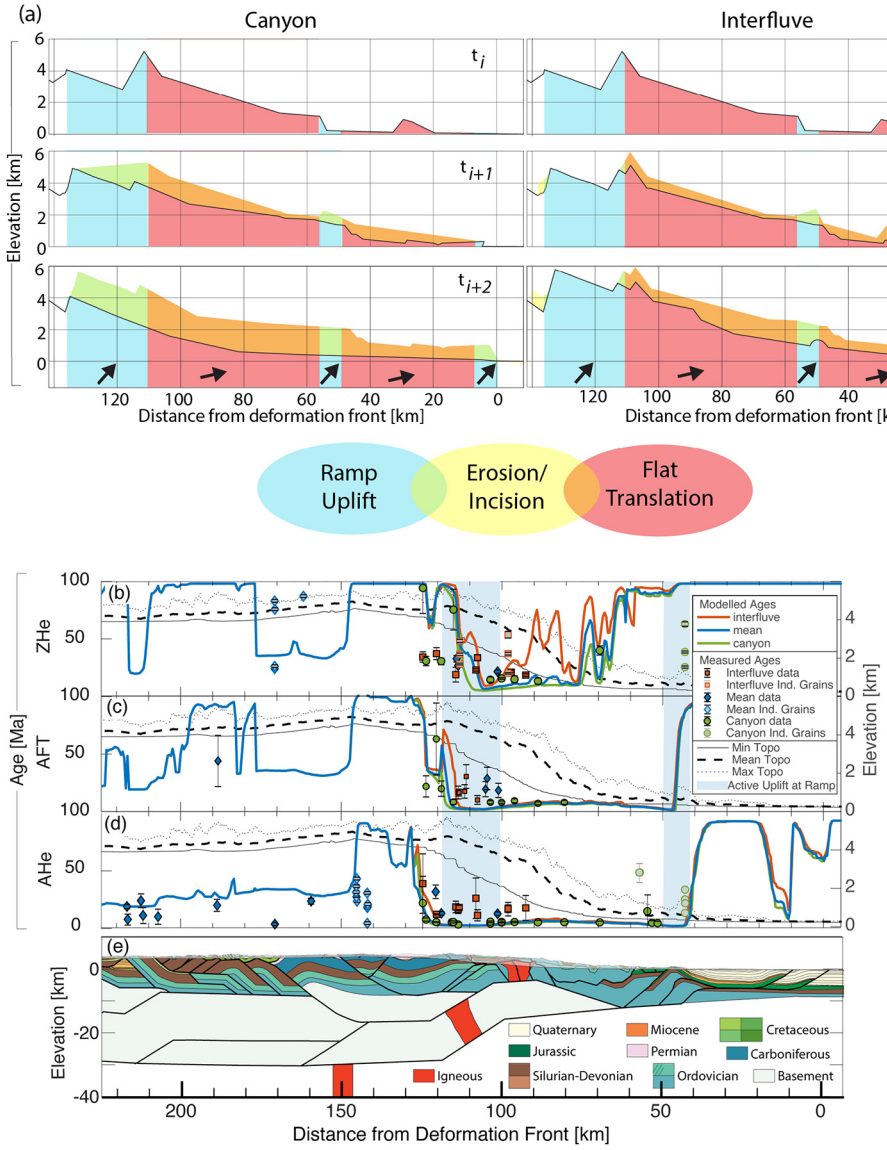

Fig. 6. (a) Schematic depicting evolution through time for canyon incision (left column) and interfluve preservation (right column). Black line that separates colours in bottom two panels represents canyon and interfluve topography (respectively). Lighter colours above line indicate eroded rock. Black arrows highlight locations of structural uplift (over ramps) and translation along flats. (b-d) Effect of incision level on modelled thermochronometric ages. Coloured line widths indicate assigned ±1 Ma error to modelled ages.

and 2.5 mm/y) to reproduce the older measured interfluve thermochronometric ages. These changes in shortening rates display the most significant difference in predicted AHe and AFT ages between ~125 and 50 km along the cross-section (Fig. 7). The fastest shortening rates of 1.0 and 2.5 mm/y produce similarly young ages as the 3 mm/y constant rate (Figs. 6b, 8). Slowing the shortening rate down to 0.25 mm/y (blue line, Fig. 7) increases the predicted AHe and AFT ages by ~15 My to 18 Ma, creating interfluve model ages that match measured ages between 120 and 80 km distance. Because the modelled rate that best fits the interfluve ages is very slow (0.25 mm/y), we tested the hypothesis of no SA ramp-driven uplift by ceasing all deformation at 12 Ma. While the cessation of shortening by 12 Ma (preceded by a constant rate of 4 mm/y) is sufficient to reproduce the interfluve measured ZHe, AFT, and AHe ages, incision starting at any proposed time (8, 4, or 2 Ma) in this scheme (e.g., in the absence of any additional shortening and associated ramp-driven uplift) is unable to match the measured canyon AHe ages, particularly over the active Subandean basement ramp at 100–120 km (Fig. S3).

5.5. Best-fit model

Based on the previous results and after evaluating a broader range of flexural and thermal model parameters (Text S2; S3), the best-fit model identified here requires the following: 1) temporally increasing effective elastic thickness (EET) from 25 to 80 km; 2) two periods of imposed surface uplift between 28–24 Ma and 19–0 Ma; 3) a radiogenic heat production of $A_0 = 2.7$ μW/m^3; and finally 4) velocity models (Figs. 8, S4) that slow down shortening rates from a background rate of 4.0 mm/y to 2.4 mm/y at 13 Ma for 6 km of shortening. Following this, shortening rates slowed further to 0.35 mm/y at 10.5 Ma for the last 10 km of shortening. This 16 km of shortening in the last 13 My is ~half of the 37 km shortening from 12 Ma–Present in the constant shortening model (Fig. 5). The best-fit model shows canyon incision initiating between 5–4 Ma and reproduces the structural geometries, basin location, and stratigraphic relationships consistent with observed geology. In addition, the predicted thermochronometric ages are largely similar to observed patterns of measured ages.

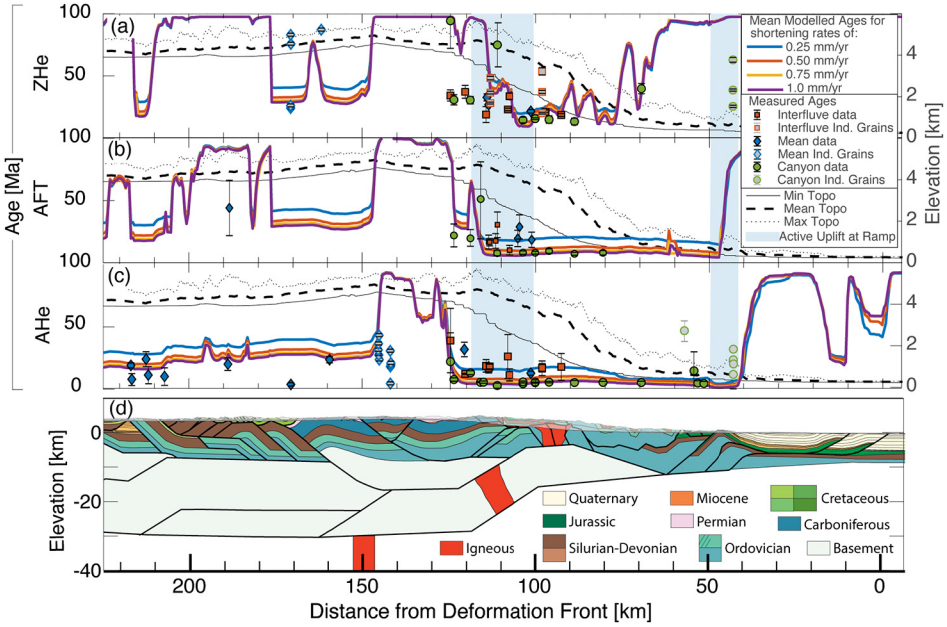

Fig. 7. Effect of SA shortening rate (0.25, 0.5, 0.75, and 1.0 mm/y) on modelled ages. Coloured line widths indicate assigned ±1 Ma error to modelled ages.

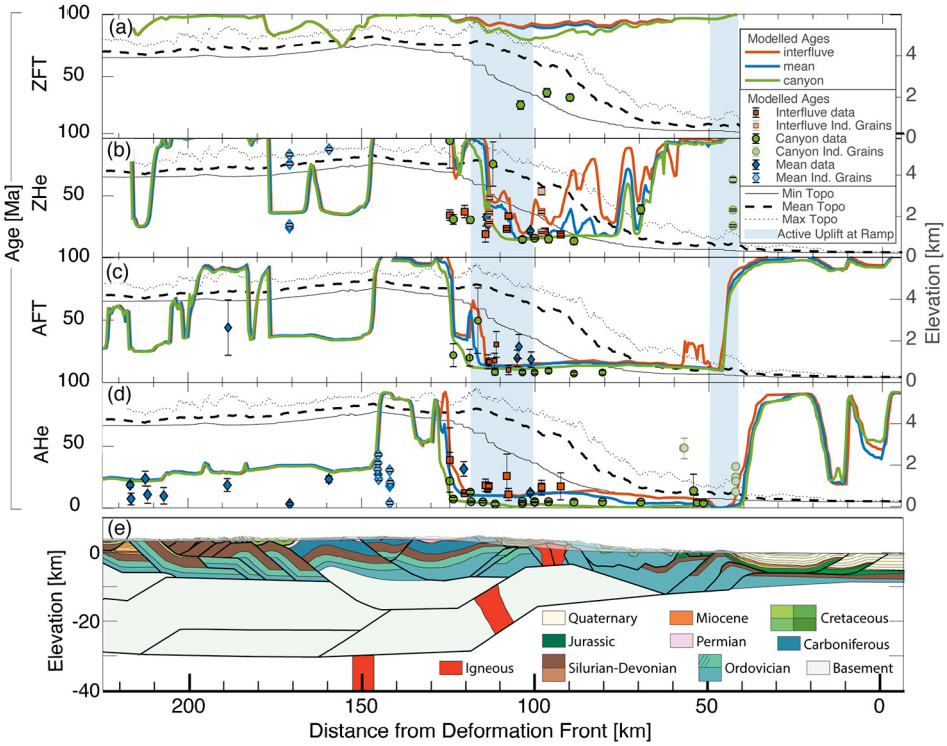

Fig. 8. Best-fit velocity with variation in magnitude of incision (i.e., interfluve, mean topography, canyon levels). Coloured line widths indicate assigned ±1 Ma error to modelled ages.

6. Discussion

6.1. Basin and thermochronometric constraints on age, location and rate of deformation

The age and thickness of synorogenic strata deposited in the AP provide key constraints on the kinematics and timing of modelled deformation from ~45–19 Ma. The best-fit model predicts a flexural basin situated to the southwest of the EC that initiated at ~48 Ma in what becomes the Altiplano depocenter (Fig. 5; 275–425 km). However, small differences in the initial shortening rate (4–6 mm/y) permit the onset of deposition to be as young as 40 Ma. The differences in age of the basal Puno Formation between the Llalli (~37 Ma) and Tinajani (~29 Ma) sub-basins suggest that these early predicted sedimentary strata were either not deposited in the southwestern Llalli Basin, or erosionally removed, and that the Ayaviri Basin was sub-divided in the location of our cross-section before 29 Ma. Uplift and erosion of the Ayaviri Basin at ~30 Ma is necessary to remove the pre-29 Ma basal portion of the Puno Formation through Upper Cretaceous strata in the Tinajani sub-basin (Figs. 1, 2). Furthermore, the boundary between the two basins preserves surface exposures of the Lower Ordovician San Jose For-

mation overlain by 24–17 Ma Tinajani Formation suggesting uplift and erosional removal of Paleozoic through Cenozoic strata (∼6+ km) prior to deposition of the Tinajani Formation at 24 Ma (Figs. 2, 3). In the model presented here, separation between the Tinajani and Llalli sub-basins, as well as the erosional removal of Paleozoic through Tertiary strata, are accomplished through motion on a basement fault moving over a ramp located between the two sub-basins (Fig. 3).

The thrust faults that bound the Tinajani sub-basin on the northeastern and southwestern sides are both accompanied by growth structures that constrain motion on these faults. The Ayaviri Fault places Middle Ordovician rocks adjacent to growth strata dated between 28–26 Ma (Perez and Horton, 2014). Growth strata measured on the southwestern side of the Tinajani sub-basin dates the Pasani Fault between 18–16 Ma (Perez and Horton, 2014). In our model with the best-fit velocity (Section 5.5), the Ayaviri Fault is active between 28.5–24 Ma, and the Pasani Fault is active at 24–22 Ma. Although the model age of final Pasani Fault motion is older than existing constraints on growth strata, this age is sensitive to the kinematics of faulting as well as the prescribed velocity. Rearranging the faulting sequence in the Altiplano permits Pasani Fault shortening from 20–18 Ma, which is at the older age limit of the measured growth strata.

The EC mean and interfluve AFT and AHe ages (15–20 Ma) and canyon ZHe ages (15 Ma) necessitate topographic uplift and exhumation at this time. Our best-fit model ties this uplift to shortening in the SA via motion on the northeastern basement fault (Fig. 5d, e), requiring SA initiation at ∼19 Ma. A slowdown in modelled shortening rates from ∼4 mm/y to ∼0.35–0.6 mm/y at ∼10 Ma reproduces both the older 15–20 Ma interfluve and mean-topography ages, and replicates the age difference between interfluve and canyon samples (Figs. 6, 8; Tables S2, S3). The cause of that slowdown may have been slab rollback and the associated westward arc retreat from its 24–10 Ma position to its modern location (Mamani et al., 2010) leading to reduced compressive stress in the overriding plate (Schellart and Moresi, 2013; Holt et al., 2015).

6.2. Persistent difference between measured and modelled ages and implications for deformation and exhumation history

There are two locations in the model where predicted ages do not match measured ages. Along the northeastern edge of the Macusani Structural Zone, a narrow 10 km zone (115–125 km, Fig. 8b) shows partially reset predicted ZHe ages as old as ∼100 Ma, while measured ZHe ages are fully reset (∼30–37 Ma; Fig. 8b). To the east, three reset ZFT ages of ∼30–36 Ma from canyon bottom samples in the Cordillera de Carabaya (90–100 km) are incompatible with predicted partially reset ZFT ages of ∼80 Ma (Fig. 8a). The mismatch between the predicted and measured ZHe and ZFT ages suggests a lack of sufficient exhumation in both of these regions. These two regions were the first to deform in the sequential model, during the first 10 My of shortening (∼50–40 Ma) when EET values are kept low (Text S2) to minimize exhumation and prevent erosion of strata that are observed at the surface.

The Macusani samples (115–125 km) were collected from units beneath the Permo-Triassic Mitu Group which is interpreted as a synrift unit, although the geodynamic conditions for this unit remain debated (Reitsma, 2012; Perez et al., 2016a; Spikings et al., 2016). The Cordillera de Carabaya samples are from Permo-Triassic plutons located directly to the east in the Zongo-San Gabán zone (Fig. 2). To reconcile the modelled and measured thermochronometric ages here, we suggest that the Mitu Graben may have been thicker than proposed by Perez et al. (2016b) and that Mitu deposits extended to the east above the preserved Permo-Triassic plutons (Fig. 2). Thickening of the Mitu Group prior to the initiation of Andean deformation would increase burial of the samples, particularly along the northeastern limb of the graben and regions to the east. If the thickness of the Mitu Group was increased by 2.5–3 km (Fig. S5), it would allow for more erosion during the flexural modelling process, permitting a higher EET during the first 10 My of modelled shortening (Text S2). More (∼4–5 km) and older erosion across the Cordillera de Carabaya from 40–30 Ma (Fig. 5b, 200–150 km, S5) is necessary to reset predicted ZFT ages (∼30–36 Ma). Finally, 2.5–3 km of additional Mitu Group strata plus early thrust burial (Glover et al., 2023) would facilitate reproducing reset ZFT ages measured in the region (Supplementary Materials, Fig. S5).

6.3. Modelled elevation history

Imposed surface uplift is included in our models for several separate reasons: the first period of imposed surface uplift limits flexural subsidence and facilitates exhumation in the AP, while the second period maintains high elevations in the AP and western EC. The second period of imposed surface uplift in our simulations is applied continuously, after AP shortening has ceased (at ∼19 Ma), in ∼0.7 km increments over the last ∼45 km of shortening. This approach maintains AP elevations at close to the modern and replicates the crustal thickening processes (e.g. Rak et al., 2017) not incorporated into the flexural modelling procedure (Text S2). Paleoelevation estimates (and associated surface uplift histories) for Peru are available from the Condoroma and Ayacucho districts along the eastern edge of the WC, in the Descanso-Yauri Basin of the AP (Fig. 2), and proximal to our cross-section in the EC (Saylor and Horton, 2014; Kar et al., 2016; Sundell et al., 2019).

In our model of the WC (proximal to the Condoroma region), slow surface uplift associated with surface faulting in the EC backthrust belt occurred (Fig. 5c) and is a source for sedimentation in the AP (e.g. Sundell et al., 2018) from 27–22 Ma. Slow, continuous topographic uplift from 27–19 Ma, combined with focused uplift on a deep-seated thrust under the Condoroma region (300 km) initiating at 19 Ma, is consistent with paleoelevation estimates indicating rapid surface uplift of the WC from 2.5 km to 4.5 km at 20–17.5 Ma (Saylor and Horton, 2014; Sundell et al., 2019) (Fig. 5e). We note that this uplift scenario does not require delamination of a lithospheric root, but rather relies upon fault-driven crustal thickening.

The southernmost basin in our model (∼275–280 km, Fig. 5d), along strike with the Descanso-Yauri Basin (Fig. 2), has a cyclic elevation history. It is initially a site of sedimentation from ∼48–32 Ma (Fig. 3b) (e.g. Sundell et al., 2018). It is then elevated to ∼3.5 km elevation passively as the southernmost basement thrust sheet is active between ∼32–28.5 Ma (Fig. 5c) and then gradually sinks back to ∼1 km in elevation at ∼24 Ma, until it is uplifted again to 4+ km in elevation when the AP shortening is active between 27 and 19 Ma. This basin's elevation of >3 km is maintained until present-day by our imposed surface uplift history, contiguous with ∼2 km of sediment accumulating in a closed basin (e.g. Kar et al., 2016). Paleoelevation proxies combined with sediment accumulation are consistent with the northernmost Altiplano Basin at low elevations to ∼23 Ma (Sundell et al., 2018, 2019). Potential elevation paths include gaining modern elevations by 17 Ma, elevation gain between ∼15–10 Ma (Sundell et al., 2019), and rapid elevation gain between 10–5.4 Ma (Kar et al., 2016). While modern elevations at 17 Ma are directly consistent with our model, the age and magnitude of model-predicted surface uplift is imposed following 19 Ma. Alternatively, instead of a continuous ∼0.7 km increase in elevation at each deformation step to maintain elevations from ∼18 Ma to Present, the AP can be allowed to naturally subside to ∼1–2 km elevation until ∼14 or 10 Ma, followed by imposed surface uplift to match paleoelevation proxies by ∼10 or

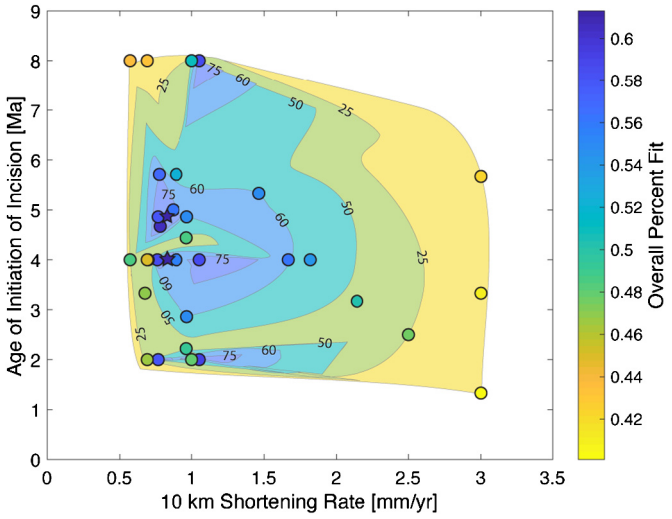

Fig. 9. Percent fit plot for all tested velocities and incision ages (Text S4, Tables S2, S3). Contours are in percentiles. Best-fit models are indicated by star.

5 Ma (Kar et al., 2016; Sundell et al., 2019). These potential elevation paths do not affect our predicted thermochronometric ages, as the absolute elevation does not affect the predicted ages.

Although imposed surface uplift (to replicate geodynamic processes such as thickening via lower crustal flow, e.g. Eichelberger et al., 2015; Garzione et al., 2017) is required to maintain elevations in the AP and the westernmost EC, topographic uplift in the northeastern portion of the EC, as well as surface uplift of the southwestern WC, are independent of the imposed uplift or subsidence history. For the EC, the active SA basement ramp controls the elevation history of rocks transported over the ramp. The ~4.5+ km elevation gained during ramp-driven uplift (and exhumation) separates the elevation history of the eastern EC from the elevation history of the backthrust belt or Altiplano Plateau to the southwest. This basement ramp influences thermochronometric ages in the eastern EC. Topographic uplift due to the active SA basement ramp has been ongoing from 19 Ma to Present and generated elevations of >4 km since ~13 Ma. This result is consistent with paleoaltimetry estimates that suggest elevations of 2.5 km at 25 Ma, 3.5 km at 17 Ma and modern elevations by 10 Ma (Sundell et al., 2019).

6.4. Proposed mechanisms and timing of incision

Proposed drivers of incision in northeastern Peru include a marked change in climate (Lease and Ehlers, 2013), plateau uplift (Garzione et al., 2017; Kar et al., 2016; Whipple and Gasparini, 2014), and endorheic basin capture (Gérard et al., 2021a,b). Our best-fit model is a combination of plateau-scale surface uplift (imposed surface uplift), structurally-driven uplift (uplift and exhumation above footwall ramp), and independently driven incision (the last steps of our model include canyon topography). Lease and Ehlers (2013) propose shortening within the EC ceased in the middle Miocene (~12 Ma) based on thermal modelling of ~15 Ma ZHe ages. They argued young (~4 Ma) measured AHe ages were then a function of ~1.0–1.6 km of canyon incision occurring at ~4.1–2.8 Ma, in the absence of uplift and due to an increase in Pliocene precipitation. Our models evaluated canyon incision between 2 and 8 Ma and obtained equally good fits to young AHe ages within this age range (Fig. 9). All models require incision to accompany slow but ongoing SA ramp uplift between 15 Ma and Present. Incision (initiating at 8, 4, or 2 Ma) in the absence of ramp uplift is insufficient to produce the young reset AHe ages present in the upper 20 km of the canyon, directly over the proposed ramp (100–120 km) (Figs. 8, S3). Instead of 15 Ma cooling due to ongoing shortening in the EC and associated exhumation, our results suggest that the ~15 Ma canyon ZHe ages are a function of SA ramp uplift and exhumation that initiated at ~19 Ma in our best-fit model (Figs. 4, 8). While incision is required to match the measured thermochronometric ages between 120–80 km (particularly AHe and ZHe ages) (Fig. 8), the driver of this incision cannot be independently determined by this study.

7. Conclusions

The thermokinematically modelled balanced cross-section presented here reproduces measured thermochronometric ages from the AHe, AFT, and ZHe systems. Our model permits an initial age of deformation in the northernmost Eastern Cordillera between 50–40 Ma, with background shortening rates between 3.0 and 5.0 mm/y. Ages and rates of deformation of the Eastern Cordillera and Altiplano are primarily constrained by patterns of synorogenic sedimentation in hinterland basins. Sedimentation occurs in the Altiplano region for the duration of the model but is both interrupted and exhumed during periods of deformation, simulating measured strata in the Ayaviri Basin. Early (48–29 Ma) sedimentation in the Tinajani Basin is removed between 28.5 and 25.4 Ma by basement uplift separating the Llalli and Tinajani sub-basins, followed by the subsequent deposition of the Puno Formation on this unconformity in conjunction with motion on the Ayaviri Fault. Ages and rates of deformation in the Subandean Zone are set by measured thermochronometric ages across the eastern Eastern Cordillera. Our thermal model highlights the need for a slowdown in shortening rates from background rates of 4.0 mm/y to between 0.25 and 0.5 mm/y from ~10 Ma to Present. This is needed to match measured canyon and interfluve thermochronometric ages, possibly reflecting a decrease in upper plate compression during slab steepening. A model with no structural uplift in the Eastern Cordillera does not match the young measured AHe ages. Canyon incision, which is independent in age from ramp-driven uplift (initiated at 19 Ma), is necessary in combination with slow shortening rates to reproduce the range in measured thermochronometer ages.

CRediT authorship contribution statement

Victoria M. Buford Parks: Writing – original draft, Validation, Methodology, Investigation, Funding acquisition, Formal analysis. **Nadine McQuarrie:** Writing – review & editing, Validation, Supervision, Project administration, Methodology, Investigation, Funding acquisition, Conceptualization. **Sarah Falkowski:** Writing – review & editing, Validation, Investigation, Funding acquisition, Conceptualization. **Nicholas D. Perez:** Writing – review & editing, Methodology. **Todd A. Ehlers:** Writing – review & editing, Validation, Supervision, Resources, Conceptualization.

Declaration of competing interest

The authors declare that they have no known competing financial interests or personal relationships that could have appeared to influence the work reported in this paper.

Data availability

Data will be made available on request.

Acknowledgements

Supporting data are included in the supporting information files. This work was supported by NASA headquarters under the NASA Earth and Space Science Fellowship program - Grant

80NSSC17K0388 to V.M.B.; National Science Foundation (NSF) Grant EAR-1842172 to N.M. and Deutsche Forschungsgemeinschaft (German Research Foundation) grant FA 1489/1-1 to S.F. We thank Midland Valley and Petex for support and use of the program *Move*. This manuscript benefitted from thoughtful discussions over the years with Mary Braza, Paul Eizenhöfer, Chloë Glover, Brad Parks and Kelin Whipple. Willi Kappler (University of Tübingen) is thanked for support with conducting modelling simulations. Andrea Stevens Goddard and two anonymous reviewers are thanked for their constructive comments that helped improve the manuscript.

Appendix A. Supplementary material

Supplementary material related to this article can be found online at https://doi.org/10.1016/j.epsl.2023.118355.

References

Brandon, M.T., Roden-Tice, M.K., Garver, J.I., 1998. Late Cenozoic exhumation of the Cascadia accretionary wedge in the Olympic Mountains, northwest Washington State. Geol. Soc. Am. Bull. 110, 985–1009. https://doi.org/10.1130/0016-7606(1998)110<0985:LCEOTC>2.3.CO;2.

Braun, J., 2003. Pecube: a new finite-element code to solve the 3D heat transport equation including the effects of a time-varying, finite amplitude surface topography. Comput. Geosci. 29, 787–794. https://doi.org/10.1016/S0098-3004(03)00052-9.

Braun, J., 2002. Quantifying the effect of recent relief changes on age-elevation relationships. Earth Planet. Sci. Lett. 200, 331–343. https://doi.org/10.1016/S0012-821X(02)00638-6.

Braza, M.E., McQuarrie, N., 2022. Determining the tempo of exhumation in the eastern Himalaya: Part 1. Geometry, kinematics, and predicted cooling ages. Basin Res. 34, 141–169. https://doi.org/10.1111/bre.12615.

Buford Parks, V.M., McQuarrie, N., 2019. Kinematic, flexural, and thermal modelling in the Central Andes: unravelling age and signal of deformation, exhumation, and uplift. Tectonophysics 766, 302–325. https://doi.org/10.1016/j.tecto.2019.06.008.

Carlotto, V., 2013. Paleogeographic and tectonic controls on the evolution of Cenozoic basins in the Altiplano and Western Cordillera of southern Peru. Tectonophysics 589, 195–219. https://doi.org/10.1016/j.tecto.2013.01.002.

Cerrón, F., Chacaltana, C., 2003. Memoria descriptiva de la revisión y actualización del cuadrángulo de Ayaviri (30-u), Escala 1:50.000. Instituto Geologico y Metalurgico del Peru (INGEMMET).

Clark, A.H., Farrar, E., Kontak, D.J., Langridge, R.J., Arenas, M.J.F., France, L.J., McBride, S.L., Woodman, P.L., Wasteneys, H.A., Sandeman, H.A., Archibald, D.A., 1990. Geologic and geochronologic constraints on the metallogenic evolution of the Andes of southeastern Peru. Econ. Geol. 85, 1520–1583. https://doi.org/10.2113/gsecongeo.85.7.1520.

Ehlers, Todd A., 2023. Pecube-D: thermokinematic and erosion modeling software for problems in tectonics and surface processes (1.0 (stable)). Zenodo. https://doi.org/10.5281/zenodo.7785668.

Eichelberger, N., McQuarrie, N., Ryan, J., Karimi, B., Beck, S., Zandt, G., 2015. Evolution of crustal thickening in the central Andes Bolivia. Earth Planet. Sci. Lett. 426, 191–203. https://doi.org/10.1016/j.epsl.2015.06.035.

Eizenhöfer, P.R., McQuarrie, N., Shelef, E., Ehlers, T.A., 2019. Landscape response to lateral advection in convergent orogens over geologic time scales. J. Geophys. Res., Earth Surf. 124, 2056–2078. https://doi.org/10.1029/2019JF005100.

Falkowski, S., Ehlers, T.A., McQuarrie, N., Glover, C.O., Perez, N.D., Buford Parks, V.M., 2023. Exhumation and incision of the eastern Central Andes, southern Peru: low-temperature thermochronology observations. Earth Planet. Sci. Lett. https://doi.org/10.1016/j.epsl.2023.118299. In press.

Farley, K.A., 2000. Helium diffusion from apatite: general behavior as illustrated by Durango fluorapatite. J. Geophys. Res., Solid Earth 105, 2903–2914. https://doi.org/10.1029/1999JB900348.

Farrar, E., Clark, A.H., Kontak, D.J., Archibald, D.A., 1988. Zongo-San Gabán zone: Eocene foreland boundary of the Central Andean orogen, northwest Bolivia and southeast Peru. Geology 16, 55–58. https://doi.org/10.1130/0091-7613(1988)016<0055:ZSGNZE>2.3.CO;2.

Gasparini, N.M., Whipple, K.X., 2014. Diagnosing climatic and tectonic controls on topography: Eastern flank of the northern Bolivian Andes. Lithosphere 6, 230–250. https://doi.org/10.1130/L322.1.

Garzione, C.N., McQuarrie, N., Perez, N.D., Ehlers, T.A., Beck, S.L., Kar, N., Eichelberger, N., Chapman, A.D., Ward, K.M., Ducea, M.N., Lease, R.O., Poulsen, C.J., Wagner, L.S., Saylor, J.E., Zandt, G., Horton, B.K., 2017. Tectonic evolution of the central Andean plateau and implications for the growth of plateaus. Annu. Rev. Earth Planet. Sci. 45, 529–559. https://doi.org/10.1146/annurev-earth-063016-020612.

Gérard, B., Audin, L., Robert, X., Gautheron, C., van der Beek, P., Bernet, M., Benavente, C., Delgado, F., 2021a. Pliocene river capture and incision of the northern Altiplano: Machu Picchu, Peru. J. Geol. Soc. 178, 11. https://doi.org/10.1144/jgs2020-100.

Gérard, B., Robert, X., Audin, L., Valla, P.G., Bernet, M., Gautheron, C., 2021b. Differential exhumation of the Eastern Cordillera in the central Andes: evidence for south-verging backthrusting (Abancay Deflection, Peru). Tectonics 40. https://doi.org/10.1029/2020TC006314.

Ghoshal, S., McQuarrie, N., Huntington, K.W., Robinson, D.M., Ehlers, T.A., 2023. Testing erosional and kinematic drivers of exhumation in the central Himalaya. Earth Planet. Sci. Lett. 609, 118087. https://doi.org/10.1016/j.epsl.2023.118087.

Gilmore, M.E., McQuarrie, N., Eizenhöfer, P.R., Ehlers, T.A., 2018. Testing the effects of topography, geometry and kinematics on modeled thermochronometer cooling ages in the eastern Bhutan Himalaya. Solid Earth 9, 599–627. https://doi.org/10.5194/se-9-599-2018.

Glover, C.O., McQuarrie, N., Falkowski, S., Ehlers, T.A., 2023. Assessing drivers of high exhumation magnitudes and young cooling ages in the eastern central Andes, southern Peru (13-16°S). Earth Planet. Sci. Lett. https://doi.org/10.1016/j.epsl.2023.118281. In press.

Grove, M., Harrison, T.M., 1996. $^{40}Ar^{*}$ diffusion in Fe-rich biotite. Am. Mineral. 81, 940–951. https://doi.org/10.2138/am-1996-7-816.

Hoke, G.D., Isacks, B.L., Jordan, T.E., Blanco, N., Tomlinson, A.J., Ramezani, J., 2007. Geomorphic evidence for post-10 Ma uplift of the western flank of the central Andes 18°30′ - 22°S. Tectonics 26, 1–17. https://doi.org/10.1029/2006TC002082.

Holt, A.F., Becker, T.W., Buffett, B.A., 2015. Trench migration and overriding plate stress in dynamic subduction models. Geophys. J. Int. 201 (1), 172–192. https://doi.org/10.1093/gji/ggv011.

Horton, B.K., 2018. Sedimentary record of Andean mountain building. Earth-Sci. Rev. 178, 279–309. https://doi.org/10.1016/j.earscirev.2017.11.025.

Horton, B.K., Perez, N.D., Fitch, J.D., Saylor, J.E., 2015. Punctuated shortening and subsidence in the Altiplano Plateau of southern Peru: implications for early Andean mountain building. Lithosphere 7, 117–137. https://doi.org/10.1130/L397.1.

Jeffery, M.L., Ehlers, T.A., Yanites, B.J., Poulsen, C.J., 2013. Quantifying the role of paleoclimate and Andean Plateau uplift on river incision. J. Geophys. Res., Earth Surf. 118, 852–871. https://doi.org/10.1002/jgrf.20055.

Kar, N., Garzione, C.N., Jaramillo, C., Shanahan, T., Carlotto, V., Pullen, A., Moreno, F., Anderson, V., Moreno, E., Eiler, J., 2016. Rapid regional surface uplift of the northern Altiplano plateau revealed by multiproxy paleoclimate reconstruction. Earth Planet. Sci. Lett. 447, 33–47. https://doi.org/10.1016/j.epsl.2016.04.025.

Ketcham, R.A., Carter, A., Donelick, R.A., Barbarand, J., Hurford, A.J., 2007. Improved modeling of fission-track annealing in apatite. Am. Mineral. 92, 799–810. https://doi.org/10.2138/am.2007.2281.

Kontak, D.J., Clark, A.H., Farrar, E., Archibald, D.A., Baadsgaard, H., 1990a. Late Paleozoic-early Mesozoic magmatism in the Cordillera de Carabaya, Puno, southeastern Peru: geochronology and petrochemistry. J. South Am. Earth Sci. 3, 213–230. https://doi.org/10.1016/0895-9811(90)90004-K.

Kontak, D.J., Clark, A.H., Farrar, E., Archibald, D.A., Baadsgaard, H., 1987. Scientific communications: geochronological data for tertiary granites of the southeast Peru segment of the central Andean tin belt. Econ. Geol. 82, 1611–1618. https://doi.org/10.2113/gsecongeo.82.6.1611.

Kontak, D.J., Farrar, E., Clark, A.H., Archibald, D.A., 1990b. Eocene tectono-thermal rejuvenation of an upper Paleozoic-lower Mesozoic terrane in the Cordillera de Carabaya, Puno, southeastern Peru, revealed by KAr and $^{40}Ar/^{39}Ar$ dating. J. South Am. Earth Sci. 3, 231–246. https://doi.org/10.1016/0895-9811(90)90005-L.

Lease, R.O., Ehlers, T.A., 2013. Incision into the eastern Andean Plateau during Pliocene cooling. Science 341, 774–776. https://doi.org/10.1126/science.1239132.

Lock, J., Willett, S., 2008. Low-temperature thermochronometric ages in fold-and-thrust belts. Tectonophysics 456, 147–162. https://doi.org/10.1016/j.tecto.2008.03.007.

Mamani, M., Worner, G., Sempere, T., 2010. Geochemical variations in igneous rocks of the Central Andean orocline (13° S to 18° S): tracing crustal thickening and magma generation through time and space. Geol. Soc. Am. Bull. 122 (1–2), 162–182.

Masek, J.G., Isacks, B.L., Gubbels, T.L., Fielding, E.J., 1994. Erosion and tectonics at the margins of continental plateaus. J. Geophys. Res. 99, 13,941–13,956.

McQuarrie, N., Ehlers, T.A., 2017. Techniques for understanding fold-and-thrust belt kinematics and thermal evolution. In: Law, R.D., Thigpen, J.R., Merschat, A.J., Stowell, H.H. (Eds.), Linkages and Feedbacks in Orogenic Systems. Geological Society of America, pp. 1–30.

McQuarrie, N., Ehlers, T.A., 2015. Influence of thrust belt geometry and shortening rate on thermochronometer cooling ages: insights from thermokinematic and erosion modeling of the Bhutan Himalaya. Tectonics 34, 1–25. https://doi.org/10.1002/2014TC003783.

McQuarrie, N., Eizenhöfer, P.R., Long, S.P., Tobgay, T., Ehlers, T.A., Blythe, A., Morgan, L., Gilmore, M.E., Dering, G., 2019. The influence of foreland structures on hinterland cooling: evaluating the drivers of exhumation in the eastern Bhutan Himalaya. Tectonics 38, 1–29. https://doi.org/10.1029/2018TC005340.

Monge Miguel, R.W., Montoya Pérez, C.A., 2003. Descriptive Report of the Review and Update of the Quadrangles of Huancané (31-x), Moho (31-y) and Isla Soto (32-y). Scale 1:100,000.

Montgomery, D.R., Balco, G., Willett, S.D., 2001. Climate, tectonics and the morphology of the Andes. Geology 29, 579–582.

Mutz, S.G., Ehlers, T.A., Werner, M., Lohmann, G., Stepanek, C., Li, J., 2018. Estimates of late Cenozoic climate change relevant to Earth surface processes in tectonically active orogens. Earth Surf. Dyn. 6, 271–301. https://doi.org/10.5194/esurf-6-271-2018.

Perez, N.D., 2015. Cenozoic Deformation History of the Andean Plateau in Southern Peru: Stratigraphic, Structural, and Geochronologic Constraints. The University of Texas at Austin.

Perez, N.D., Horton, B.K., 2014. Oligocene-Miocene deformational and depositional history of the Andean hinterland basin in the northern Altiplano Plateau, southern Peru. Tectonics 33, 1819–1847. https://doi.org/10.1002/2014TC003647.

Perez, N.D., Horton, B.K., Carlotto, V., 2016a. Structural inheritance and selective reactivation in the central Andes: Cenozoic deformation guided by pre-Andean structures in southern Peru. Tectonophysics 671, 264–280. https://doi.org/10.1016/j.tecto.2015.12.031.

Perez, N.D., Horton, B.K., McQuarrie, N., Stübner, K., Ehlers, T.A., 2016b. Andean shortening, inversion and exhumation associated with thin- and thick-skinned deformation in southern Peru. Geol. Mag., 1–29. https://doi.org/10.1017/S0016756816000121.

Rak, A.J., McQuarrie, N., Ehlers, T.A., 2017. Kinematics, exhumation, and sedimentation of the North-central Andes (Bolivia): an integrated thermochronometer and thermokinematic modeling approach. Tectonics 36, 1–31. https://doi.org/10.1002/2016TC004440.

Reiners, P.W., Spell, T.L., Nicolescu, S., Zanetti, K.A., 2004. Zircon (U-Th)/He thermochronometry: He diffusion and comparisons with 40Ar/39Ar dating. Geochim. Cosmochim. Acta 68, 1857–1887. https://doi.org/10.1016/j.gca.2003.10.021.

Reitsma, M.J., 2012. Reconstructing the Late Paleozoic–Early Mesozoic Plutonic and Sedimentary Record of South-East Peru: Orphaned Back-arcs Along the Western Margin of Gondwana. PhD thesis Terre and Environment 111. University of Geneva, Switzerland, p. 226.

Sánchez, A.F., Zapata, A.M., 2003. Memoria descriptiva de la revisión y actualización de los cuadrángulos de Sicuani (29-t), Nuñoa (29-u), Macusani (29-v), Limbani (29-x), Sandia (29-y), San Ignacio (29-z), Yauri (30-t), Azángaro (30-v), Putina (30-x), La Rinconada (30-y), Condoroma (31-t), Ocuviri (31-u), Juliaca (31-v), Callalli (32-t), y Ácora (32-x). Escala 1:100 000. Instituto Geologico y Metalurgico del Peru (INGEMMET).

Saylor, J.E., Horton, B.K., 2014. Nonuniform surface uplift of the Andean plateau revealed by deuterium isotopes in Miocene volcanic glass from southern Peru. Earth Planet. Sci. Lett. 387, 120–131. https://doi.org/10.1016/j.epsl.2013.11.015.

Schellart, W.P., Moresi, L., 2013. A new driving mechanism for backarc extension and backarc shortening through slab sinking inducedtoroidal and poloidal mantle flow: results from dynamic subduction models with an overriding plate. J. Geophys. Res., Solid Earth 118 (6), 3221–3248. https://doi.org/10.1002/jgrb.50173.

Schildgen, T.F., Hodges, K.V., Whipple, P.W., Reiners, P.W., Pringle, M.S., 2007. Uplift of the western margin of the Andean plateau revealed from canyon incision history, southern Peru. Geology 35, 523–526. https://doi.org/10.1130/G23532A.1.

Sempere, T., Carlier, G., Soler, P., Fornari, M., Carlotto, V., Jacay, J., Arispe, O., Néraudeau, D., Cárdenas, J., Rosas, S., Jiménez, N., 2002. Late Permian-Middle Jurassic lithospheric thinning in Peru and Bolivia, and its bearing on Andean-age tectonics. Tectonophysics 345, 153–181. https://doi.org/10.1016/S0040-1951(01)00211-6.

Spikings, R., Reitsma, M.J., Boekhout, F., Miskovic, A., Ulianov, A., Chiaradia, M., Gerdes, A., Schaltegger, U., 2016. Characterisation of Triassic Rifting in Peru and implications for the early dissaembly of western Pangaea. Gondwana Res. 35, 124–143.

Sundell, K.E., Saylor, J.E., Lapen, T.J., Styron, R.H., Villarreal, D.P., Usnayo, P., Cárdenas, J., 2018. Peruvian Altiplano stratigraphy highlights along-strike variability in foreland basin evolution of the Cenozoic central Andes. Tectonics 37, 1876–1904. https://doi.org/10.1029/2017TC004775.

Sundell, K.E., Saylor, J.E., Lapen, T.J., Horton, B.K., 2019. Implications of variable late Cenozoic surface uplift across the Peruvian central Andes. Sci. Rep. 9, 4877.

Villegas-Lanza, J.C., Chlieh, M., Cavalié, O., Tavera, H., Baby, P., Chire-Chira, J., Nocquet, J.-M., 2016. Active tectonics of Peru: heterogeneous interseismic coupling along the Nazca megathrust, rigid motion of the Peruvian Sliver, and Subandean shortening accommodation. J. Geophys. Res., Solid Earth 121, 7371–7394. https://doi.org/10.1002/2016JB013080.

Whipp, D.M., Ehlers, T.A., Blythe, A.E., Huntington, K.W., Hodges, K.V., Burbank, D.W., 2007. Plio-quaternary exhumation history of the central Nepalese Himalaya: 2. Thermokinematic and thermochronometer age prediction model. Tectonics 26, 1–23. https://doi.org/10.1029/2006TC001991.

Whipple, K.X., Gasparini, N.M., 2014. Tectonic control of topography, rainfall patterns, and erosion during rapid post-12 Ma uplift of the Bolivian Andes. Lithosphere 6, 251–268. https://doi.org/10.1130/L325.1.

Whipple, K.X., Tucker, G.E., 1999. Dynamics of the stream-power river incision model: implications for height limits of mountain ranges, landscape response timescales, and research needs. J. Geophys. Res., Solid Earth 104 (B8), 17661–17674. https://doi.org/10.1029/1999JB900120.